actuators

*Article*

# Experimental Study on the Snowfall Flow Control of Backward-Facing Steps Using a High-Durability Designed Plasma Electrode

**Tasuku Tanaka [1], Hisashi Matsuda [2,*], Toshiki Takahashi [1], Takahiro Chiba [2], Nobuyoshi Watanabe [3], Hideaki Sato [3] and Masafumi Takeyama [3]**

[1] Graduate School of Engineering, Hokkaido University of Science, Sapporo 006-8585, Japan
[2] Laboratory of Advanced Materials for Cold Region, Hokkaido University of Science, Sapporo 006-8585, Japan
[3] Asahi Rubber Inc., Saitama 330-0801, Japan
* Correspondence: matsuda-h@hus.ac.jp; Tel.: +81-11-688-7150

**Abstract:** Using a high-durability designed plasma electrode (PA), the plasma actuation effect on both a two-dimensional backward-facing step flow (standard model) and an arc-shaped three-dimensional backward-facing step flow (arc model) was investigated experimentally. First, we searched for plasma operation control conditions suitable for the two-dimensional backward-facing step flow by carrying out experiments using a medium-sized circulating wind tunnel. Next, using the natural-snow wind tunnel of the Hokkaido University of Science, we examined whether an AC-driven PA can control snowfall flow. It became clear for the first time that the amount of snow accumulation can be reduced by more than 20% when the PA is driven at a dimensionless frequency of $fH/U$ = 0.32, where $f$ is the pulsed modulation frequency, $H$ is the step height, and $U$ is the mainstream velocity, and the duty ratio $D$ (the time ratio of PA_ON to the total time when controlled by the pulsed modulation frequency) is equal to 1.0%. It was also confirmed that by masking the arc-shaped electrode parallel to the mainstream and using only the part perpendicular to the mainstream of the PA electrode, the amount of accumulated snow could be reduced by up to 20%. It has become clear that high-durability designed plasma electrodes can control the snowfall flow and reduce the amount of accumulated snow.

**Keywords:** plasma actuator; high-durability designed plasma electrode; snowfall flow control; backward-facing step; snow accumulation reduction

check for updates

**Citation:** Tanaka, T.; Matsuda, H.; Takahashi, T.; Chiba, T.; Watanabe, N.; Sato, H.; Takeyama, M. Experimental Study on the Snowfall Flow Control of Backward-Facing Steps Using a High-Durability Designed Plasma Electrode. *Actuators* **2022**, *11*, 313. https://doi.org/10.3390/act11110313

Academic Editor: Subrata Roy

Received: 15 September 2022
Accepted: 24 October 2022
Published: 27 October 2022



## 1. Introduction

The dielectric barrier discharge (DBD) plasma actuator (PA) is easy to apply to existing machines because it does not have a mechanical driving part that causes failure, and the device can be formed with a thin-film structure. Therefore, various applications can be expected as unique airflow control devices. Review articles by Cork et al. [1] and Touchoud [2] have introduced the potential of this technology in detail, and related research is being conducted worldwide. However, the electrode configuration and shape are still being studied to improve the device's performance and expand its applications. Moreau et al. [3] summarized the research conducted in the Plasma European project and introduced fine-wire electrodes, sawtooth electrodes, sliding discharge actuators using three electrodes, and a Multi-DBD PA. Akbıyık et al. [4] investigated the effect on the stall angle and lift and drag coefficients for the NACA0015 wing using three types of PAs with different shapes (straight, sawtooth, and square). Asaumi et al. [5] conducted a wind tunnel test with a high Reynolds number ($Re$ = 6.0 × $10^5$) using a tri-electrode PA composed of three electrodes for the NACA0012 blade. They found that the induced velocity of the TED-SD-PA was more than double the induced velocity of the standard PA and reported that the control efficiency could also be improved. Wang et al. [6] increased the stall angle of the NACA0015 blade by 27.5% by using two sawtooth-shaped electrodes separated by a dielectric layer. Berendt et al. [7] conducted experiments on NACA0012 and NACA0015 blades using a Multi-DBD PA with multiple stages of saw-toothed PAs and reported that even the $Re = 10^5$ order could improve stall. Various other PA electrode shapes have also been developed. Segawa et al. [8] reported that the feedback control of the separation flow of the NACA0024 airfoil is possible using the invented string-type DBD-PA electrode and an FGB sensor. Sato et al. [9] fabricated a multistage DBDPA using the metal inkjet printing method and reported that it was possible to induce an ion wind equal to or greater than that of a conventional PA fabricated with copper tape. A method for evaluating the characteristics of the PA is also being investigated. Ashpis et al. [10] devised a new thrust measurement method that investigates the effects of stepwise changes in the drive frequency and voltage of the PA and reported points to note and issues in a comparison of different experimental environments. Furthermore, Ashpis et al. [11] investigated power measurement accuracy by focusing on shunt resistor and capacitor methods. The capacitor method was reported to be highly reliable and easy to implement. Many studies have also been conducted on how to apply PAs. Matsunuma [12] installed a DBDPA on the end wall of a linear cascade wind tunnel for the purpose of improving turbine performance at low Re numbers (Re < $10^5$) and controlled the passage vortex generated in the turbine cascade by burst driving. Detailed experimental results have been reported. CFD studies on PA actuation mechanisms have also been performed. Zhang et al. [13] reported the process from the formation of an initial thin jet immediately after the PA drive to the wall jet. In addition, Chedevergne et al. [14] conducted experiments and numerical analyses of DBD and PSJ plasma actuators and reported their respective control strategies. For the field application of the plasma actuator, the effect of the ambient pressure has also been investigated. Benard et al. [15] placed a PA in a vacuum chamber and measured and compared the velocity induced by the PA by changing the pressure from 1 atm to 0.2 atm. As a result, they reported that the induced velocity increased as the pressure decreased to 0.6 atm and, conversely, decreased at pressures below that. Their experimental results suggest that the PA can also be expected to be used at high altitudes, such as in aircraft. Intensive research has also been conducted on the effects of relative humidity and water droplets on plasma electrodes. Anderson and Roy [16] measured the thrust force of a PA attached to a flat plate in the range of 43% $\leq$ RH $\leq$ 53% and reported a slight increase in performance with increasing humidity. In addition, Benard et al. [17] investigated in detail the flow induced by a PA under a wide range of relative humidity conditions ranging from 40% $\leq$ RH $\leq$ 98% and found that the PA could be driven normally even under high-humidity conditions, but the momentum transfer performance decreased as the relative humidity increased. It was also shown that this problem could be solved by increasing the applied voltage. Wicks and Thomas [18] also systematically investigated the effect of relative humidity on a PA over a range of 20% $\leq$ RH $\leq$ 90%. There was little effect of relative humidity at RH < 40%. They reported that the thrust reduction force could be well approximated by the power of the ratio of the steam partial pressure to the saturated water vapor pressure under conditions of 40% < RH < 70% and RH > 70%. To analyze the effect of raindrops on PAs, Lilley et al. [19] conducted a study in which water droplets were sprayed directly onto PA electrodes. For two droplet size conditions (50.0–62.5 $g/m^2$ and 125–150 $g/m^2$), the PA drive was tested at two applied voltages (17.5 $kV_{pp}$ and 22.5 $kV_{pp}$) and two fundamental frequencies (10 kHz and 14 kHz), and the tendency of thrust force recovery was investigated after spraying the water droplets. It was reported that the thrust force recovered to over 40% after 5 s of spraying, and further recovery can be expected if driving for a longer time.

In applied research, Fujii et al. [20] performed LES using a high-resolution scheme for the Ahmed model, investigated influential PA installation positions, and reported that the drag coefficient could be reduced by as much as 13%. Lai et al. [21] conducted numerical simulations using a simplified car model based on the Motor Industry Research Association's standard model and an efficient global optimization algorithm and reported that a drag reduction rate of 13% or more could be achieved. Research on its application to the field of aviation is also active. Zainuddin et al. [22] summarized the findings in a review article, comparing the findings of each study. Keisar et al. [23] conducted an experiment on a full-size V-tail model and confirmed the improvement of take-off performance with the PA drive for its application to uncrewed aerial vehicles. In addition, Sekimoto et al. [24] conducted a flight test under natural conditions for a small uncrewed aerial vehicle and reported that the PA drive could improve stall even at high pitch angles. Xie et al. [25] investigated the effect of μs-pulsed plasma control on a symmetrical flight wing and reported that it could increase lift and decrease drag. In an application to wind turbine blades, Matsuda et al. [26] conducted research on the control of the flow around the blades by a PA drive for the wind turbines of large wind turbines (1.75 MW) and suggested that a PA drive is also effective for improving the performance of larger wind turbines. More recently, Tanaka et al. [27] used a plasma electrode (length 8 m, thickness 2 mm, and width 60 mm) with high durability designed by Asahi Rubber Inc. for a 300 kW medium-sized wind turbine (turbine diameter 33 m) and confirmed that the front-edge separation was suppressed. The plasma actuation technology increased the wind turbine torque. It was analyzed statistically, showing that the plasma airflow control effect is practical even for a large wind turbine's operating range ($Re > 10^6$). Furthermore, Aono et al. [28] investigated the effect of a DBD-PA on the 3D flow of a small wind turbine through numerical simulation and found that the shaft torque increased by about 19%. Ogawa et al. [29] performed numerical simulations of the NACA0015 airfoil flow using a DBD-PA and confirmed good flow control with feedback control based on pressure fluctuations from a single-point pressure sensor.

To expand the application of PA control, researchers from the Delft Institute of Technology and a research group in China are conducting research to control snow accretion by the thermal action of a PA driven at high speed to prevent the icing of wind turbine blades, etc. [30–32]. On the other hand, Matsuda et al. [33] conducted a weather resistance evaluation of the plasma electrode in collaboration with Asahi Rubber Inc., which is developing a plasma electrode with high-durability performance, and reported that the PA was expected to work even in a heavy-snow environment and also confirmed that the conventional AC-driven PA could affect the snowfall flow. However, at the time, the PA electrode provided on the leading edge of the wing was covered with snow early, so no clear difference could be found in snow accumulation control by the PA drive. Snow in winter in cold regions adheres not only to wind turbines but also to automobiles and railcars, causing snow damage that hinders regular operation. The research results of Matsuda et al. [33] are expected to open a new genre of snowfall control as a promising application of PA control. Therefore, in this study, we focused on the effect of controlling the snowfall flow of PA and investigated whether it is possible to suppress snow accumulation by using a driving PA. Our target was set around the railcar door, where snow accretion damage is noticeable. A test was planned by assuming that the flow around the center of the railcar door is a two-dimensional backward-facing step flow and that the door corner, where heavy snowfall is conspicuous, is a three-dimensional arc-shaped backward-facing step flow. Figures 1 and 2 show an overview of the modeled backward-facing step flow for the snow accumulation around the railcar door and the flow in the center of the door. First, we searched for suitable PA control conditions for a two-dimensional backward-facing step flow by performing experiments using a medium-sized circulating wind tunnel. Next, using the natural-snow wind tunnel at the Hokkaido University of Science, we investigated whether an AC-driven PA could control the snowfall flow against a two-dimensional backward-facing step flow and a three-dimensional arc-shaped backward-facing step flow and whether the amount of snow accumulation could be reduced by the AC-driven PA.

**Figure 1.** Snow accumulation conditions.

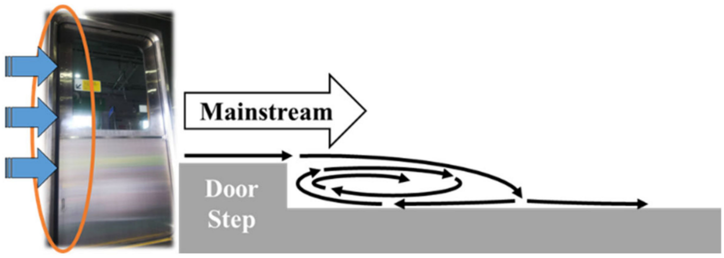


**Figure 2.** Modeling of flow around railcar door.

## 2. Materials and Methods

### 2.1. Wind Tunnels

Two types of wind tunnels were used in the test. First, using a circulating wind tunnel (EBARA CORPORATION, maximum wind speed 30 m/s, test unit 400 mm × 400 mm), oil flow visualization (Sections 3.1 and 3.4), PIV measurement (Section 3.2), and fluctuation velocity measurement using a hot-wire anemometer (Section 3.3) were performed to investigate the suitable driving conditions for the PA. Figure 3 shows the circulating wind tunnel.

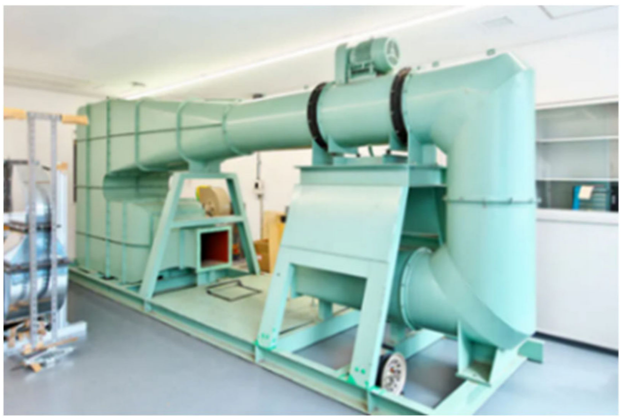

**Figure 3.** Circulating wind tunnel.

In winter, a natural-snow wind tunnel owned by the Hokkaido University of Science (Wind Engineering Center Co., Ltd., Tokyo, Japan, maximum wind speed 18 m/s, test unit 1 m × 1 m) was used for a special PIV measurement (Section 3.5.1), and snow accumulation tests (Section 3.5.2) were conducted. Please note that this special PIV measurement uses dry snowflakes as tracers. The snow inlet at the top of the natural-snow wind tunnel is equipped with a stiff plastic rotating brush, and the number of rotations can be controlled. In addition, the test room where the natural-snow wind tunnel is installed can control the room temperature down to −10 °C. Figure 4 shows the natural-snow wind tunnel.


**Figure 4.** Natural-snow wind tunnel.

*2.2. Test Models*

Two models were used for wind tunnel tests. One is a standard model in which the flow near the center of the railcar door is assumed to be a two-dimensional backward-facing step flow. The other is an arc model that assumes a three-dimensional arc-shaped backward-facing step flow at the door corner of a railcar, where snow accumulates significantly. The arc shape is based on the shape of the actual railcar used by the Hokkaido Railway Company. Figure 5 shows the outline of the railcar door and modeling sites, Figure 6 shows the standard model, and Figure 7 shows the arc model. For the shape of the standard model, following Matsuda et al. [34], we designed the maximum thickness of the model to be 40 mm, the length was 715 mm, and the width was 500 mm. The tip has a 10: 1 elliptical shape and forms a step portion through a 100 mm flat-plate portion. The step height $H$ was 25 mm. The arc model is based on the standard model and has a step shape with a corner bend. Note that the Reynolds number was defined as $Re = UH/\nu$, where $\nu$ is the kinematic viscosity of air.

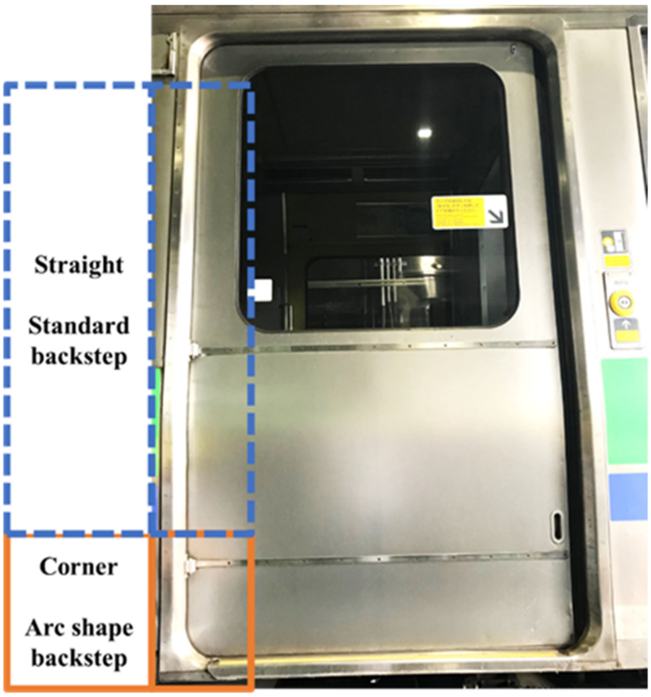


**Figure 5.** Modeling sites around the railcar door.

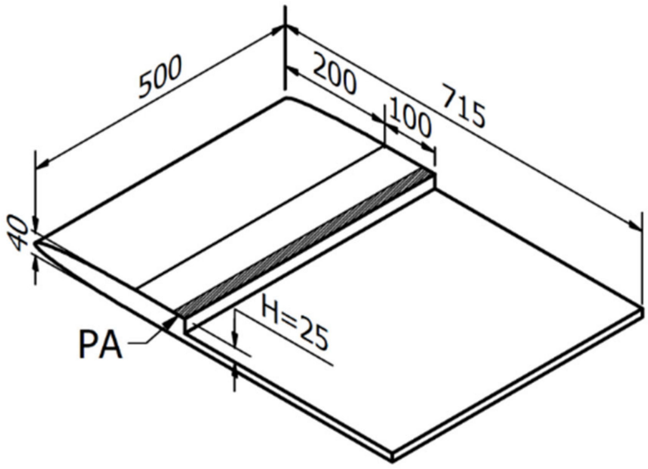


**Figure 6.** Standard model.

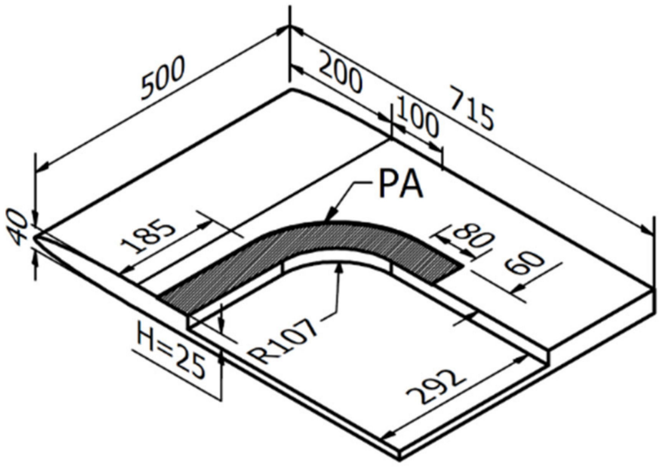


**Figure 7.** Arc model.

Both models were designed using CAD and printed for each part with an FDM 3D printer (Shenzhen Creality 3D Technology Co., Ltd., Shenzhen, China, Ender3pro and Shenzhen Tronxy Technology Co., Ltd., Shenzhen, China, X5SA). For each model, the PA mounting position (step part) was designed by cutting down the thickness of the plasma electrode to minimize the effect of the thickness of the electrode on the flow. As the slicer software, Ultimaker Cura 5.0 was used with a partition wall thickness of 2 mm and a filling rate of 20%. The assembled parts were bonded using an adhesive (Araldite). Then, the model surface was smoothed so as not to affect the wind tunnel tests. Orville Thunder (Koki Holdings Co., Ltd., Tokyo, Japan, FSV10SA) was used for surface polishing, and sandpaper No. 2000 was employed. Figure 6 shows a schematic overview of the standard model. Figure 7 shows the outline of the arc model.

### *2.3. High-Durability Designed Plasma Electrodes (Asahi Rubber Inc.) and the PA Electrode Drive Control Condition*

The total thickness of the highly durable plasma electrode is 1.1 mm. Silicone rubber with 0.4 mm thickness was used as the dielectric, and a 50 μm thick titanium thin film was used as the electrode, resulting in a highly durable structure. A linear-type electrode was used for the standard model, and an arc-shaped-type electrode was used for the arc model. Figure 8a,b show overviews of the standard electrode (Figure 8a) and the arc-shaped electrode (Figure 8b), respectively.

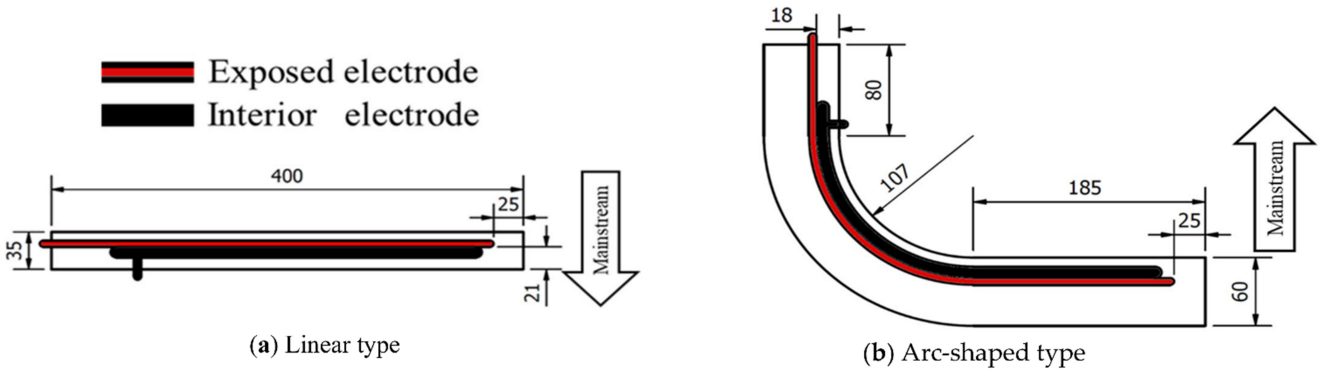


**Figure 8.** High-durability designed plasma electrodes.

For the control of the backward-facing step flow, it has been reported that it is more effective to drive the PA in pulsed modulation mode to synchronize with the periodic structure in the separated shear layer [34]. Figure 9 shows the outline of pulsed modulation control. The PA is driven by the fundamental frequency $F$ [Hz], and the time ratio of PA_ON to the total time when controlled by the pulsed modulation frequency $f$ [Hz] is defined as the duty ratio $D$ [%]. The dimensionless frequency $f+ = fH/U$ is defined as the dimensionless pulsed modulation frequency with the step height $H$ = 25 mm and a mainstream velocity $U$ [m/s]. In this study, the applied voltage was fixed at $V$ = 8 kVpp, and the fundamental frequency was fixed at $F$ = 50 kHz, changing both the duty ratio and the pulsed modulation frequency. In addition, the plasma actuation effect on the flow controls was investigated. Figure 10 shows the oscillation status of the PA recorded using a high-voltage probe (Pintek Electronics Co., Ltd., New Taipei City, Taiwan, HVP-39PRO) and a current monitor (U.R.D., Ltd., Kanagawa, Japan, CTL-28-S90- 5Z-1R1). The power consumption of the electrodes was 51.1 W/m ($f$ = 96 Hz, $D$ = 1.0%).

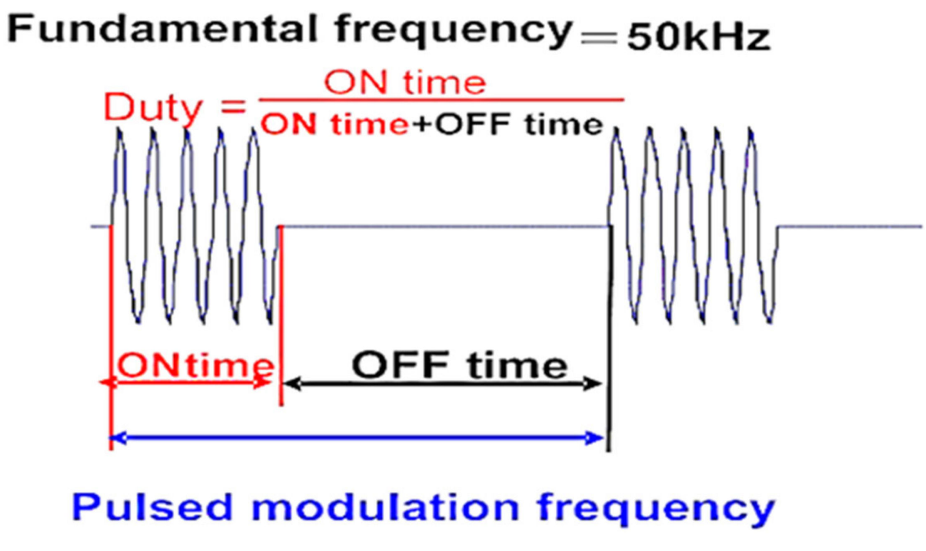


**Figure 9.** Pulse Modulation Control Overview.

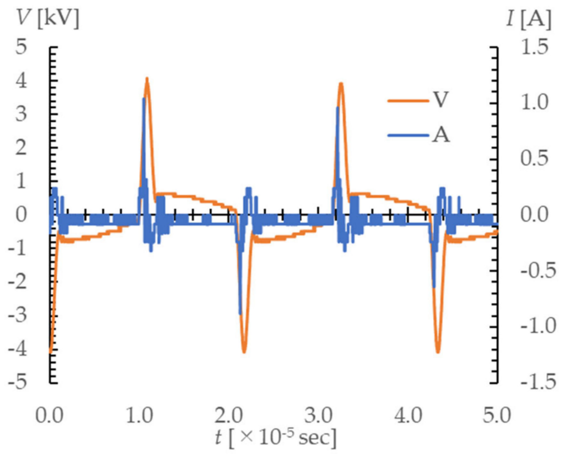


**Figure 10.** Oscillation status of the PA.

## 3. Experimental Results

### 3.1. Oil Flow Visualization (Standard Model, Circulating Wind Tunnel)

First, the primary flow field with PA_OFF was studied using the standard model. Then, suitable control conditions were evaluated from the change in the reattachment length due to the PA drive. For the oil flow visualization test, oil mixed with liquid paraffin, titanium oxide, and oleic acid was used at about 15:5:4 (weight ratio). Figure 11 shows the oil flow pattern with PA_OFF. The reattachment point (red line) was determined from the oil flow pattern where the flow stagnates (equivalent to a velocity of 0). The reattachment length $L$ [mm] is defined as the distance from the stagnation point to the corner edge of the model. The wind speed U was set to 25 m/s (90 km/h, $Re = 4.1 \times 10^4$), which is equivalent to the running velocity of the actual railcar. The inlet turbulence intensity measured with an I-type hot-wire probe (DANTEC DY NAMICS A/S, Skovlunde, Denmark, type55R01) was 0.80% at 100 mm from the leading edge of the standard model and 100 mm from the leading edge of the model at an inflow wind speed of 25 m/s.

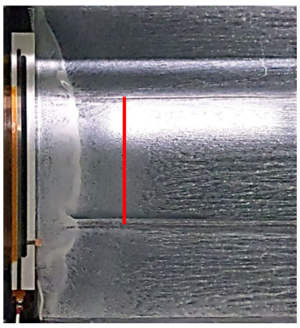

**Figure 11.** Oil flow pattern.

The reattachment length for PA_OFF was about 5.6 $H$ (140 mm $\pm$ 1.1 mm). The reattachment distance was evaluated from a set of five oil flow images. Urita et al. [35] reported 5.2 $H$, and Matsuda et al. [34] reported 5.8 $H$ in a similar flow field, suggesting that a standard two-dimensional backward-facing step flow could be formed in this test as well. Note that side plates (plastic plates) were attached to both ends of the model in the oil flow visualization test to ensure two-dimensionality. It was confirmed that the two-dimensionality of the flow was maintained over the central part of 200 mm. The two-dimensionality was 100 mm when the side plate was not attached.

Second, the effect of the duty ratio on the reattachment length was investigated. The PA was driven at $D$ = 1.0, 5.0, 10.0, 15.0, 20.0, 25.0, and 30.0%, and the changes in the reattachment length were compared. The dimensionless frequency was set at $f+$ = 0.32. Figure 12 shows the change in the reattachment length with the duty ratio. It was confirmed that the PA drive reduced the reattachment length. It was also confirmed that the effect was the most effective when $D$ = 10 to 20%, and the reattachment length was reduced by up to 12.5%.

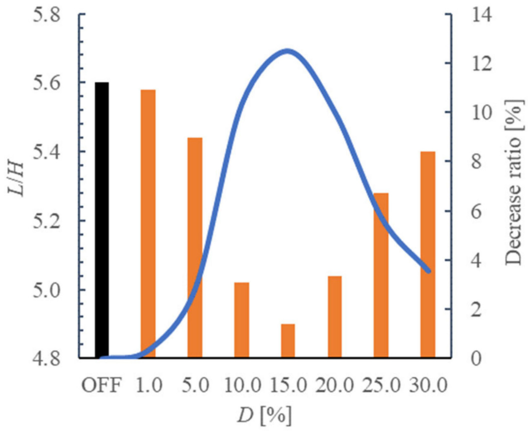


**Figure 12.** Reattachment length against duty ratio.

Next, the effect of the dimensionless frequency on the reattachment length was investigated. The PA was driven at the dimensionless frequencies $f+$ = 0.1, 0.2, 0.32, 0.4, and 0.5 to investigate changes in the reattachment length. The duty ratio was set to $D$ = 15.0%, where the reattachment length was most affected. Figure 13 shows the change in the reattachment length with the dimensionless frequency $f+$. It was confirmed that dimensionless frequencies from $f+$ = 0.3 to 0.4 are effective for the backward-facing step flow. From these facts, in this study, suitable driving conditions for the PA of the standard model were set to $D$ = 10 to 20% and dimensionless frequency $f+$ = 0.32.

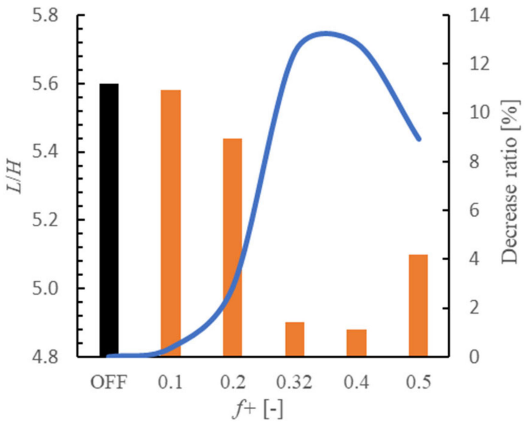


**Figure 13.** Reattachment length against dimensionless frequency.

### *3.2. PIV Measurement Using Micro Soap Bubbles (Standard Model, Circulating Wind Tunnel)*

In this section, we investigate the effect of the PA drive on the velocity field based on PIV measurements using micro soap bubbles as tracers. Note that this section only considers the standard model. A micro soap bubble generator developed by Shibata et al. was used as a tracer generator for PIV measurements. More than 50% of the diameters of soap bubbles emitted from this generator were 0.9 mm ± 0.1 mm. From the PIV measurement results, it was confirmed that good followability to steady flow was required [36]. A 2.5 W laser beam (Shenzhen Scotle Technology Co., Ltd., Guangdong, China, YPS-P3370-25) was used as the light source for PIV measurement, and a cylindrical lens (Thorlabs Japan Inc., Tokyo, Japan, LK1087L2-A) was used to form a sheet and illuminate it from above. The flow field near the step of the model was measured. The behavior of micro soap bubbles was photographed with a high-speed camera (KATOKOKEN Co., Ltd., Kanagawa, Japan, K7-USB) and processed with PIV software (KATOKOKEN Co., Ltd., Kanagawa, Japan, FlowExpert2D2C-L). The shooting angle of view was 200 mm × 200 mm, the pixel count was 320 × 320, and the frame rate was 2000 fps. The measurement conditions were such that 5 to 10 particles could be captured in the inspection range (60 × 70 pixels). The step height was 25 mm, and 40 pixels were supported. FlowExpert2D2C-L, used for PIV processing, has an algorithm that eliminates error vectors with correlation coefficients, average brightness, and velocity differences in eight neighborhoods. By using micro soap bubbles as tracers, PIV measurement was possible even at a wind speed of 20 m/s (72 km/h, $Re = UH/\nu = 3.3 \times 10^4$), which is equivalent to the running conditions of actual railcars.

Figure 14a,b show the velocity gradient (d$U$x/d$Y$) distribution near the step in the PA_OFF (Figure 14a) and PA_ON (Figure 14b) cases. $U$x represents the streamwise component of the velocity, and $Y$ represents the perpendicular distance from the step surface. The PA was driven at $D$ = 10.0% and $f$+ = 0.32, the preferable control conditions in which the reattachment length was minimized in the oil flow visualization test. Compared to PA_OFF, a region with a larger velocity gradient (d$U$x/d$Y$) value was observed along the interface of the separated shear layer downstream of the step end for PA_ON cases (Figure 14b). These facts indicate that the PA drive narrows the streamline spacing; that is, the velocity increases in the separated shear layer. This finding agrees with Matsuda et al. [37], who controlled the separation flow around the NRELS825 blade by using a PA drive and found that the PA drive formed an acceleration region in the separated shear layer.

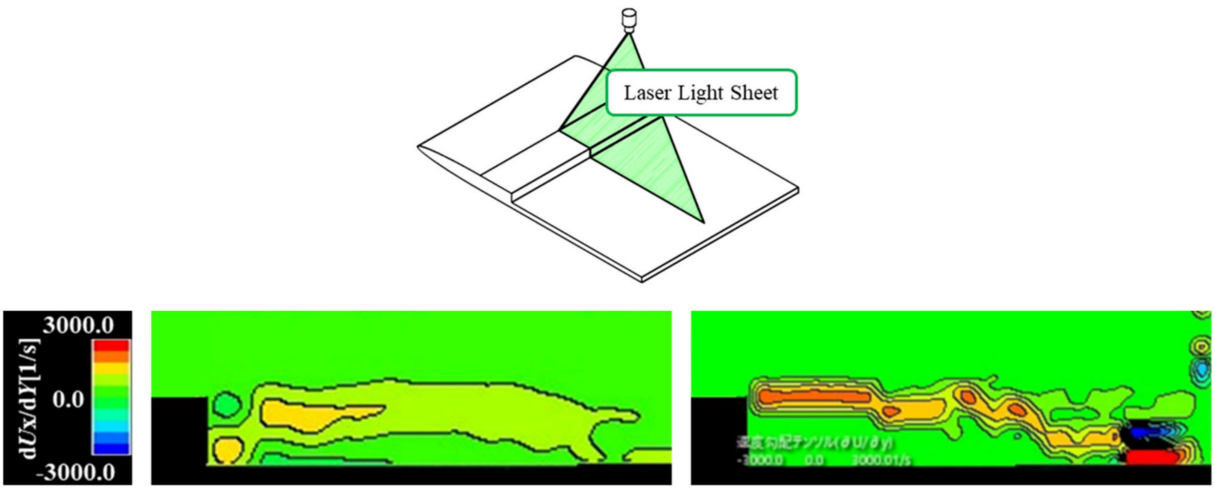


(a) PA_OFF (b) PA_ON [$D$ = 10.0%, $f$+ = 0.32]

**Figure 14.** Iso-d$U$x/d$Y$ map.

*3.3. FFT Analysis: Investigation of Periodic Structure in Separation Shear Layer (Standard Model, Circulating Wind Tunnel)*

Next, the periodic structure in the separated shear layer driven by the PA was investigated to investigate the control mechanism of the PA. The signal sent from the hot-film probe (DANTEC DYNAMICS A/S, type55R01) was input to the oscilloscope (RIGOL TECHNOLOGIES CO., LTD, DS1054Z) via a flow velocity signal processor (DANTEC DYNAMICS A/S, MiniCTA54T30), and the measurement data were converted into a CSV file at a sampling rate of 10 kHz. The measurement position was set at the point at which the velocity increased during the use of the PA drive in the PIV measurement test, namely, 1 $H$ backward from the step ends with 1 $H$ height. After that, the measurement data were analyzed using spectrum analysis software (SPCANA Ver4.8). Calibration velocities were obtained with a simple hot-fire anemometer (Testo SE & Co., KGaA, Titisee-Neustadt, Germany, tes-to425). To consider the effect of the temperature rise of the airflow during the experiment, the velocity calibration of the hot-film anemometer was performed at 3 m/s intervals in the range of 4 to 25 m/s both before and after the measurement. Velocity fluctuation measurements were taken at a mainstream wind velocity of $U$ = 20 m/s (72 km/h, $Re = 3.3 \times 10^4$), which is the same as in the PIV measurement. With the PA drive condition fixed at $f+$ = 0.32, the effect of the duty ratio was investigated at $D$ = 1.0, 5.0, 10.0, and 15.0%. Figure 15 shows the results of the FFT analysis. Peaks at 520 Hz, 260 Hz, and 750 Hz are predominant as characteristic frequencies. These peak frequencies correspond to double, one, and three times the pulsed modulation frequency ($f$ = 256 Hz) during the use of the PA drive. This means that the periodic components of pulsed modulation are enhanced within the separation shear layer during the use of the PA drive. In addition, we can see in Figure 15 that the larger the duty ratio, the higher the power spectral density of the peak frequency obtained. These facts confirm that performing pulsed modulation control that synchronizes with the periodic structure in the separated shear layer is an effective PA drive condition.

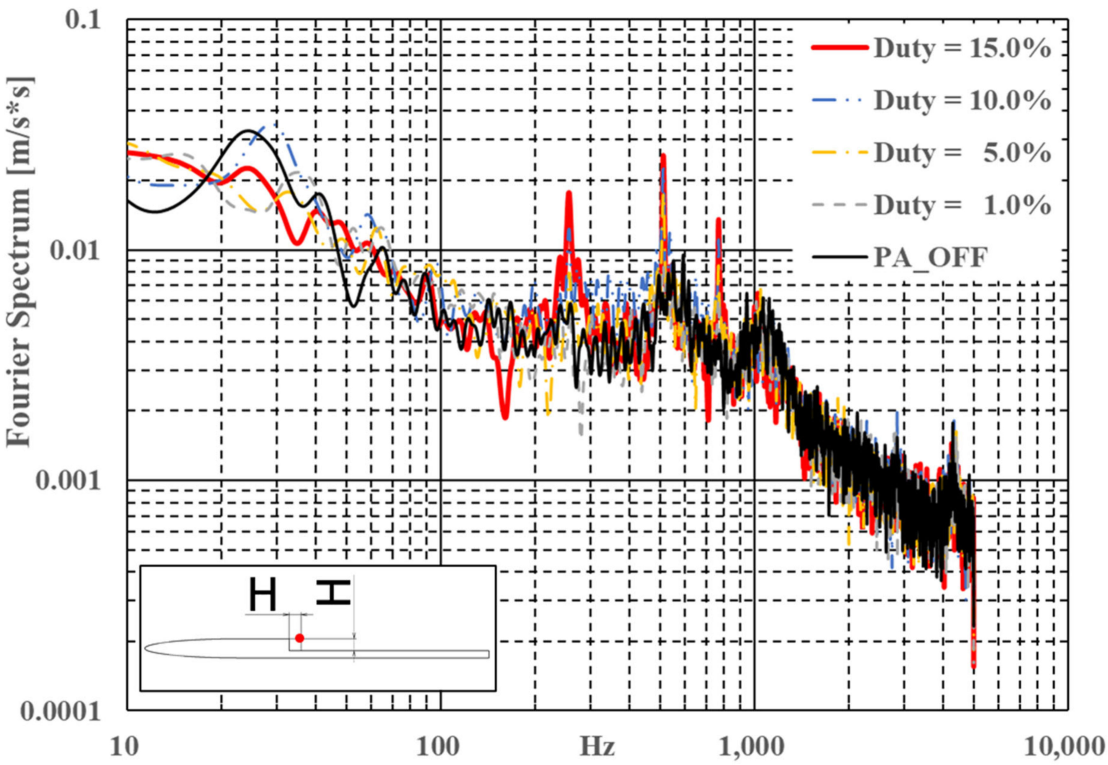


**Figure 15.** FFT Analysis (Fourier Spectrum).

### *3.4. Oil Flow Visualization (Arc-Shaped Model, Circulating Wind Tunnel)*

In this experiment, using the arc model, we investigated the PA drive effect on the flow around the arc-shaped backward-facing step. The PA was driven at a dimensionless frequency of $f+$ = 0.32 and $D$ = 15.0%. Figure 16a,b show the results of the PA_OFF case (Figure 16a) and PA_ON case (Figure 16b), respectively. Figure 17 shows the snow accretion of the arc-shaped portion of the real railcar door corner in winter. Compared with the oil flow pattern of PA_OFF (Figure 16a) and Figure 17, both figures show a very similar crescent-shaped morphology along the corner bend. Therefore, it is judged that the snow accretion phenomenon of the railcar door portion is closely related to the separation flow phenomenon of the arc-shaped backward-facing step. With plasma actuation, the reattachment area decreased by about 10 mm at the model's center. It was confirmed that the separation flow could be controlled, even with arc-shaped plasma actuation.

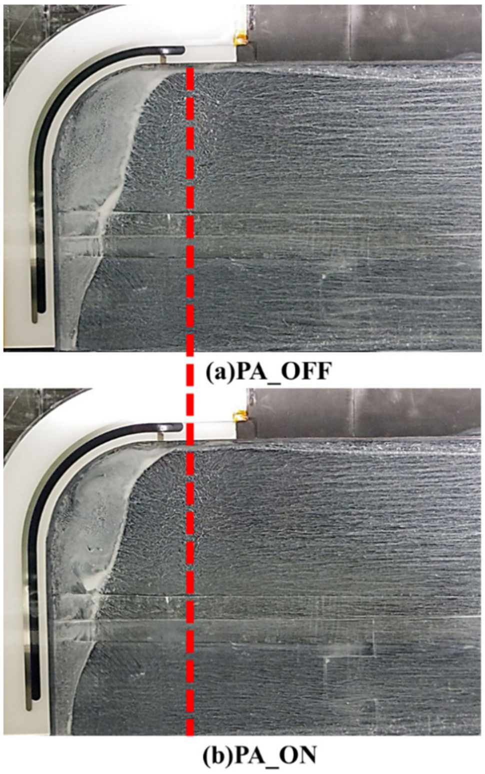


**Figure 16.** Oil flow visualization result.

**Figure 17.** Snow deposition on actual train door.

*3.5. Natural-Snow Wind Tunnel Test*

Next, we conducted a wind tunnel experiment using the natural-snow wind tunnel to investigate whether the PA-driven snowfall control shown by Matsuda et al. [33] is possible even with the backward-facing step flow. The falling snow quality changes with only slight differences in the weather. Therefore, the natural-snow wind tunnel tests were carried out under different snowfall conditions over two years. First, the snow density was measured to manage the quality of falling snow. The snow density was measured using a polyester vessel (54 L, 1.24 kg). The wind velocity during the PIV measurement and the snow accumulation test was 7.5 m/s (27 km/h, $Re = 1.4 \times 10^4$). This is because when the wind velocity is higher, the snowfall flow blows through the upper part of the test model due to the structure of the natural-snow wind tunnel, so it was adjusted so that the entire test model would be exposed to snow.

3.5.1. PIV Measurement Using Dry Snowflakes as Tracers (Standard Model)

The PIV measurement was performed using dry snowflakes as tracers, and the effect of the PA drive on the snowfall flow around the standard model was investigated. Please note that this PIV measurement uses dry snowflakes as tracers and examines the behavior of snowflakes rather than airflow. Since it is known that powder snow is more suitable for PIV measurement [33], natural snow that had just fallen was collected when the temperature was low. Figure 18 shows the process of dry snow collection. On days when it was difficult to obtain dry snow (powder snow), the collected snow was placed in a test room in a −5 °C atmosphere for one day to obtain appropriate natural snow. Next, to eliminate the unevenness of the snow quality, the collected snow was blended to realize the same snowfall conditions to the greatest extent possible. The snow density was adjusted to 160 to 180 kg/m$^3$. Figure 19 shows the process of snow injection during the natural-snow wind tunnel test. In the PIV measurement, a 4 W laser sheet was irradiated from above, and the behavior of the dry snowflake was photographed with a high-speed camera (Vision Research Inc., NJ, USA, PhantomV1212). Figure 20 shows the process of PIV measurement using natural snowflakes as tracers. Figure 21 shows the behavior of snowflakes captured by the high-speed camera. The PA was driven at $D$ = 1.0, 5.0, 10.0, 15.0, and 20.0%. The dimensionless frequency was set to $f+$ = 0.32. The obtained data were processed with the same PIV software (KATOKOKEN Co., Ltd., Kanagawa, Japan, FlowExpert2D2C-L) as was used for the microbubble PIV measurement. The shooting angle of view was 560 mm × 350 mm, the pixel count was 1280 × 800, and the frame rate was 4000 fps. The measurement conditions were such that 5 to 10 particles could be captured in the inspection range (60 × 70 pixels). The step height was 25 mm, and 57 pixels were supported. Snowflakes in the main flow section were advected at approximately the same velocity as the main flow velocity. Snowflake velocities at 9 $H$ (Figure 22) from the step surface were examined for five cases when the main flow wind speed was set to 7.5 m/s. The variation error of the snowflake advection velocity was 7.5 m/s ± 0.13 m/s, confirming that the measurements were highly reproducible.

**Figure 18.** Process of snow collection.

**Figure 19.** Process of snow injection during the test.

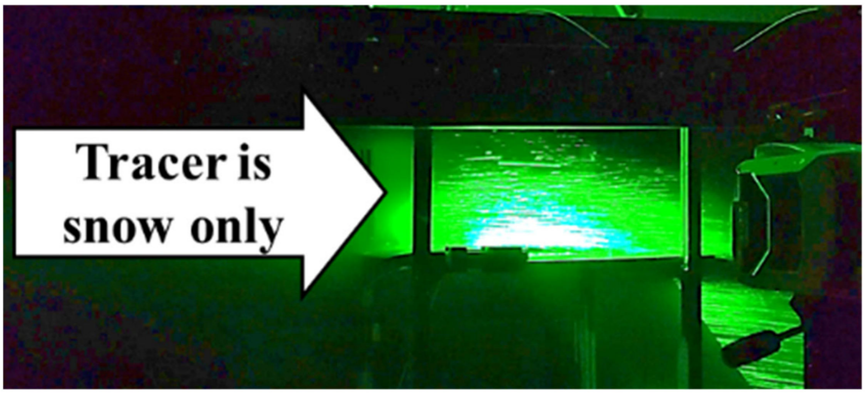


**Figure 20.** PIV measurement using snowflakes.

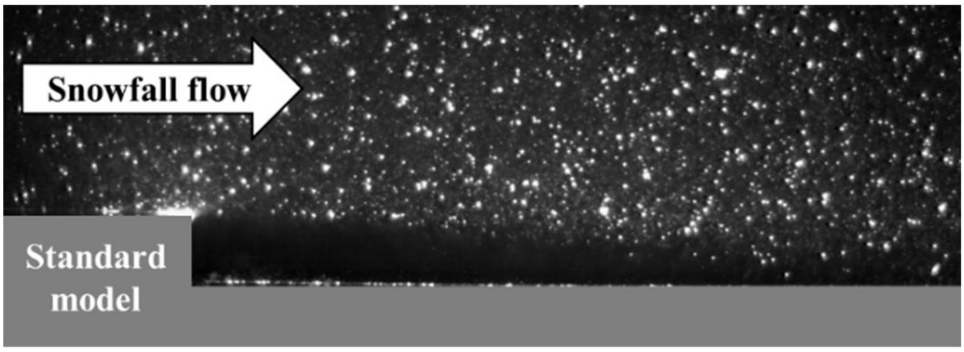


**Figure 21.** Snow behavior photographed by the high-speed camera.

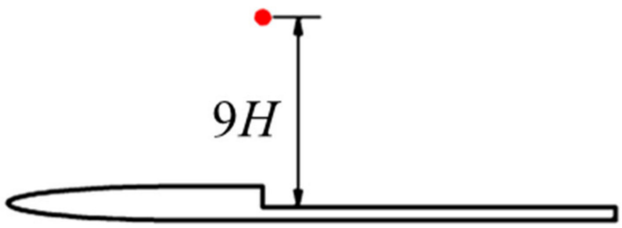


**Figure 22.** Monitoring point of snowflake velocity.

Velocity Distribution (Streamwise Component: Ux)

The change in the reattachment length of the snowfall flow was investigated from the velocity distribution obtained by PIV measurement using snowflakes as tracers. Figure 23 shows the snowflake velocity distribution of the streamwise component for PA_OFF (Figure 23a) and PA_ON (Figure 23b–e). To clarify the reattachment point, the streamwise component of the PIV measurement result was binarized. The red region indicates the positive values, and the blue region indicates the negative values of the streamwise component. Therefore, the downstream edge of the blue region shows the reattachment point of the snowflake flow. The reattachment length of $D$ = 1.0% was 4.4 $H$, almost the same as PA_OFF. On the other hand, when the PA was driven at $D$ = 5.0 to 30.0%, the reattachment length was reduced in each case. It was confirmed that we could control the snowfall flow and reduce the reattachment length with the PA drive.

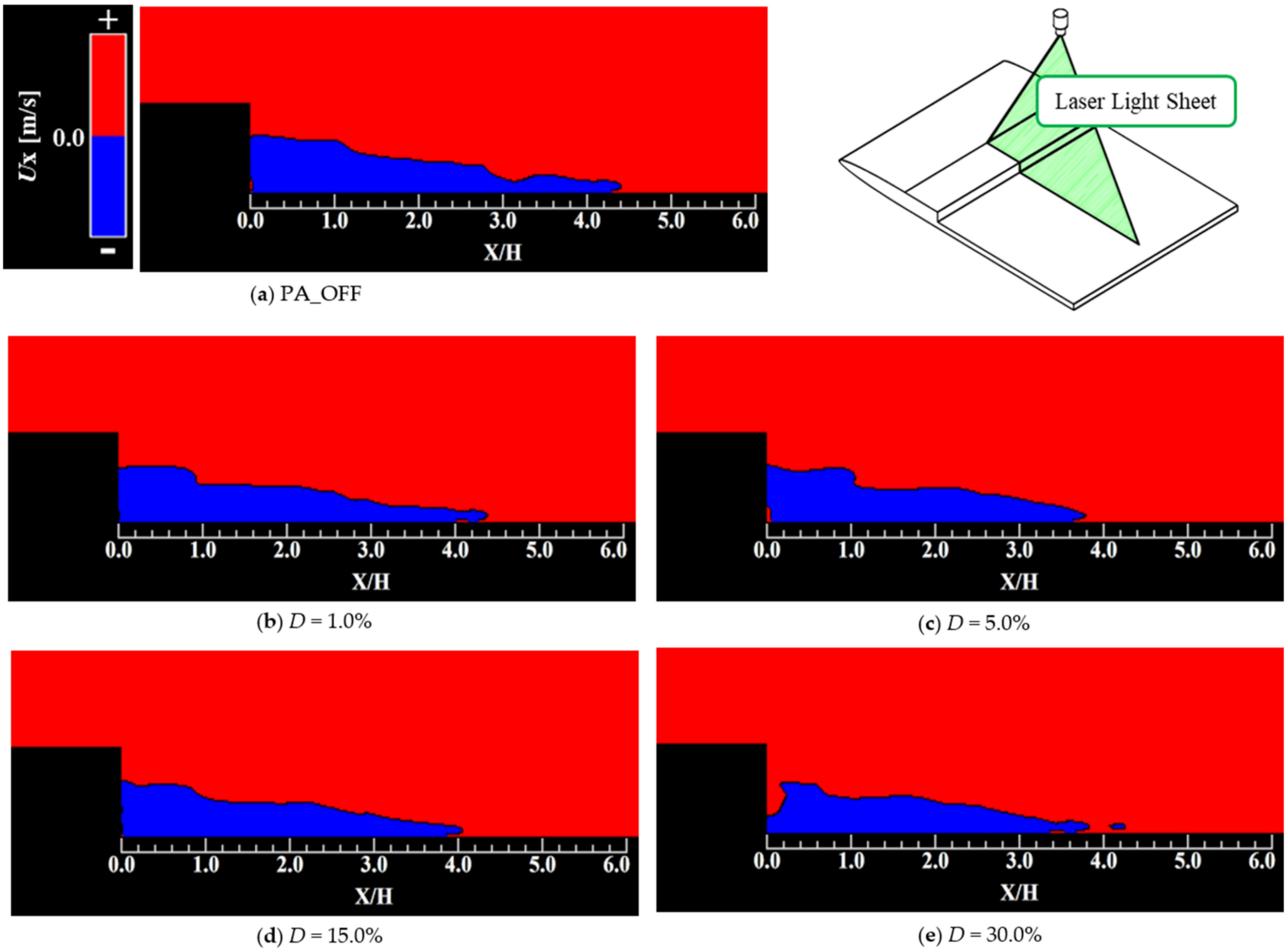


**Figure 23.** Iso-*U*x map (PIV results using dry snowflakes as tracers).

Velocity Gradient (dUx/dY)

Subsequently, the change in the velocity field around the separation shear layer was investigated. Figure 24 shows the velocity gradient (d*U*x/d*Y*) distribution for PA_OFF (Figure 24a) and PA_ON (Figure 24b–e). Remember that these PIV results were obtained by using snowflakes as tracers. Under all measurement conditions, red and yellow regions, which indicate regions with a larger velocity gradient of the snowflakes, were observed at the interface of the separated shear layer. The interesting point is that even if $D$ = 1.0% occurs there, the red and yellow regions extend downstream of the separated shear layer. This corresponds to the fact that in the case of airflow PIV measurement using soap bubbles as tracers, an increasing velocity region was generated in the separated shear layer by the PA drive (Section 3.2). The extension of the larger d*U*x/d*Y* area in the downstream direction was almost the same regardless of $D$, which ranged from 1.0% to 30.0%. It was confirmed again that plasma actuation affects not only the separated airflow but also the movement of snowflakes during snowfall.

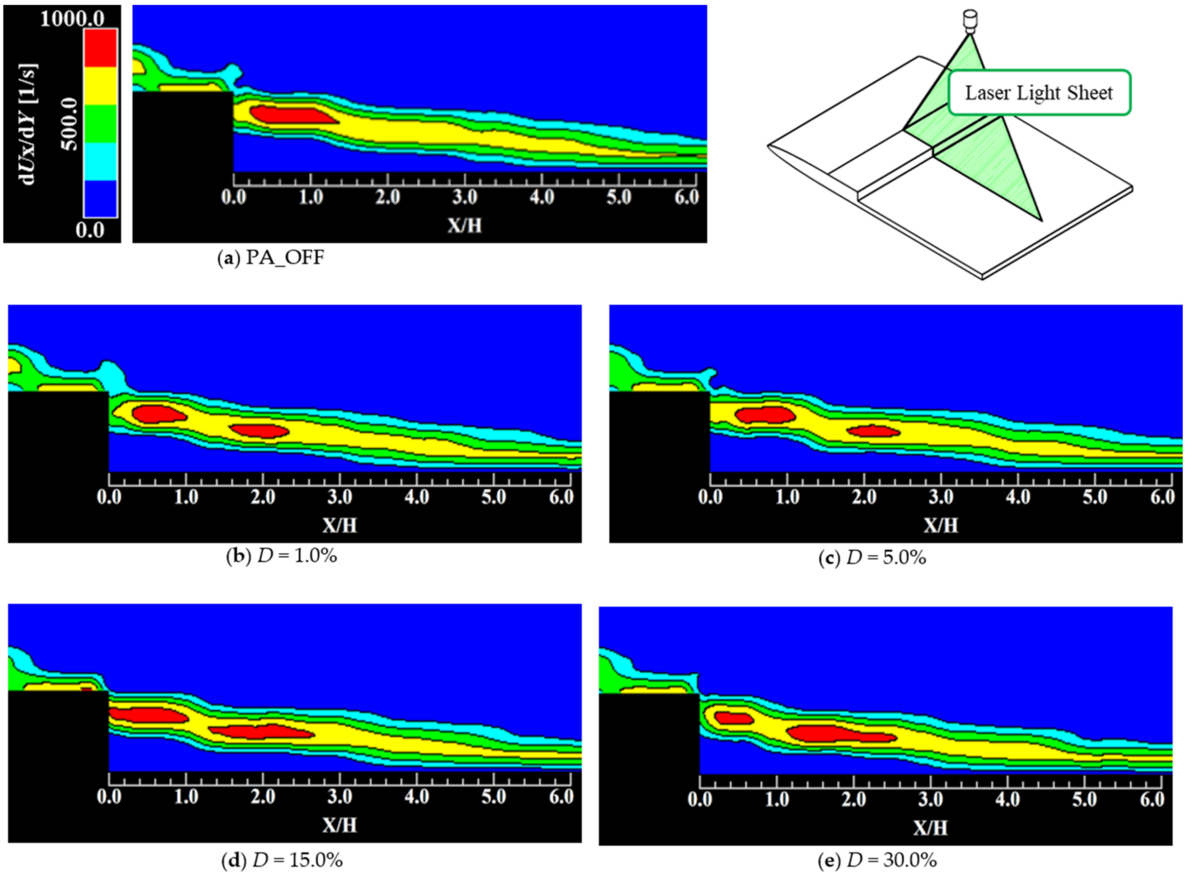


**Figure 24.** Iso-d$Ux$/d$Y$ map (PIV results using dry snowflakes as tracers).

### 3.5.2. Snow Accumulation Test

Since it was found in the previous experiment that PA control is possible for snowfall flows, we next examined the PA actuation effect on the snow deposition around the standard model using wet snow. Finally, a snow accumulation test was conducted over two years using wet snow. For the snow quality in the snow accumulation test, we required fresh wet snow able to form a snowball. However, since old snow (a few days after snowfall) collapses and becomes like fine ice, even if snow is added, it does not deposit onto the test model. Therefore, the measurement was carried out while waiting for new snowfall. In addition, to eliminate the unevenness of the snow quality, the collected snow was blended to realize the same test conditions to the greatest extent possible. When it was judged that the degree of wetness was insufficient in the snow accumulation test, we tried to create a wet snow state by leaving it at room temperature for a while. In the snow accumulation test, we adjusted the density of the snow to 210 to 240 kg/m$^3$. In the snow accumulation test, two basins were added in 2 min. This corresponds to an accelerated test condition of about 250 times the average maximum daily snowfall (30 cm/24 h) in winter in Sapporo. The snow accumulation situation was photographed using a GOPRO (TAJIMA MOTOR CORPORATION., Tokyo, Japan, HERO8). Due to the limited period of use of the natural-snow wind tunnel and the difficulty in obtaining wet snow from fresh snow, only two duty ratio conditions, namely, $D$ = 1.0% and 15.0%, were tested. The former corresponds to the most energy-saving condition, and the latter corresponds to the most affected in the oil flow visualization test. The dimensionless frequency during the use of the PA drive was $f+$ = 0.32.

#### Snow Accumulation Test in 2021 (Standard Model)

In 2021, only PA_OFF and PA_ON ($D$ = 1%) were compared due to the limitation on the use of the natural-snow wind tunnel facility. Figure 25 shows the snow accumulation situation 120 s after the onset of snowfall. Looking at the snow accumulation situation with PA_OFF, snowflakes accumulate in white downstream of the back step. On the other hand, in the PA_ON case, the amount of snowfall is smaller than in the PA_OFF case. As mentioned above, in this test, we tried to achieve the same quality of snowfall conditions as much as possible, so it is considered that the result of this experiment shows that the PA drive can suppress the amount of snow accumulated in the backward-facing step flow. It is presumed that the PA drive formed an increasing velocity area on the separated shear layer, causing snowflakes to be brushed away.

(**a**) PA_OFF (**b**) PA_ON

**Figure 25.** Snow accumulation test [120 s] (2021).

Snow Accumulation Test in 2022 (Standard Model)

Next, the snow accumulation test results in 2022, during which the temperature was lower than in 2021 and there was a lot of lighter snow, are described. In this test, to quantitatively evaluate the amount of snowfall, the snowfall image taken from the upper part of the test piece using a GOPRO was binarized with image editing software (GIMP2). Moreover, the black-and-white ratio of the output image was used with OpenCV. Using calculations, the change in the amount of snowfall was investigated. Before the binarization process, the threshold was changed to 100 and narrowed down to the range where snowflakes could be clearly seen. Figures 26 and 27 show the PA_OFF and PA_ON snow accumulation tests. Tables 1 and 2 show the percentage decrease in PA_OFF and PA_ON snow accumulation tests. During the tests shown in Figures 26 and 27, the snow accumulation behavior was significantly different due to the difference in snow quality, but it was confirmed that the amount of snow accumulation was reduced by driving the PA. The amount of snow accumulated could be reduced by up to 19%. It was quantitatively confirmed that the snow accumulation suppression effect is exhibited when the PA is driven.

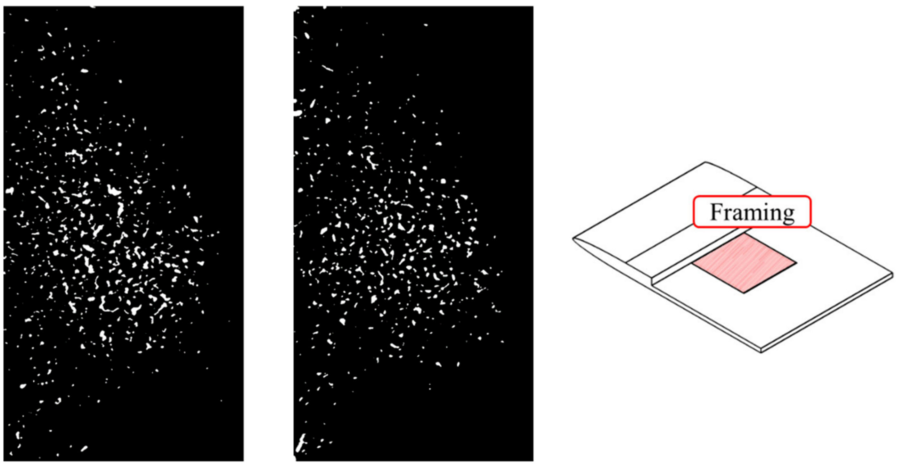


(**a**) PA_OFF (**b**) $D = 15.0\%$

**Figure 26.** Snow accumulation test (standard model) [Result_1].

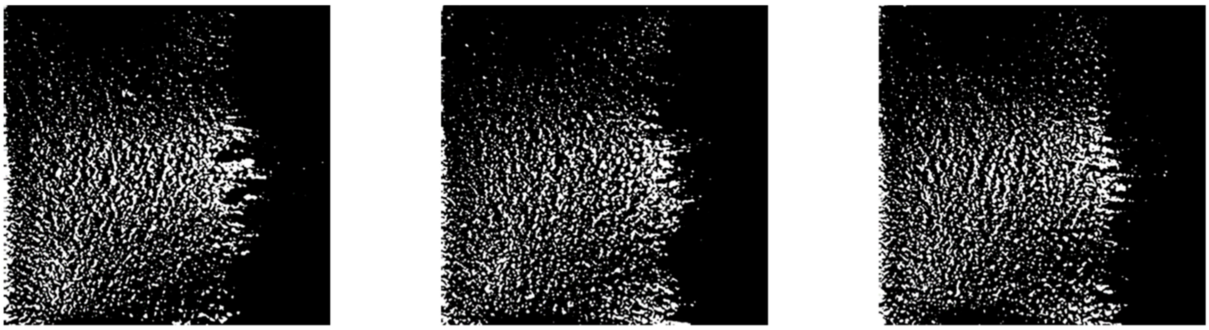

(**a**) PA_OFF (**b**) $D$ = 1.0% (**c**) $D$ = 15.0%

**Figure 27.** Snow accumulation test (standard model) [Result_2].

**Table 1.** Snow accumulation test (standard model) [Result_1].

| Duty | Off | 15.0% |
|---|---|---|
| White ratio [%] | 3.60 | 2.91 |
| Rate of decrease [%] | - | −19.17 |

**Table 2.** Snow accumulation test (standard model) [Result_2].

| Duty | Off | 1.0% | 15.0% |
|---|---|---|---|
| White ratio [%] | 13.68 | 12.84 | 13.31 |
| Rate of decrease [%] | - | −6.14 | −2.70 |

Snow Accumulation Test in 2022 (Arc Model)

In the arc-shaped model, the PA was driven at $D$ = 15.0% and compared with PA_OFF. Figure 28 compares the results of the PA_OFF and PA_ON snow accumulation tests. The threshold was set at 100. Like the standard model test, the image after the snow accumulation test was binarized to quantitatively examine the amount of snow accumulation. The amount of snow accumulated increased in the case of the arc-shaped model when driving the PA. This was the opposite of what was expected before the test.

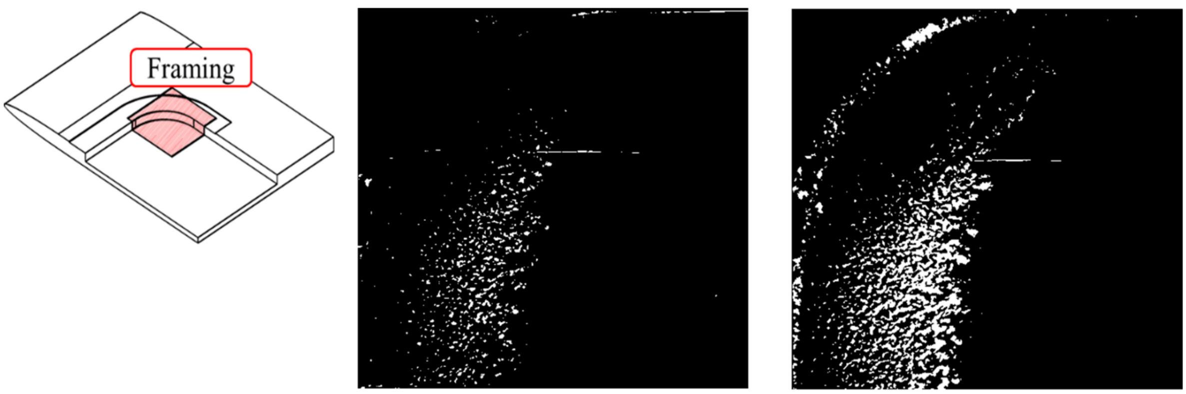


(**a**) PA_OFF (**b**) $D$ = 15.0%

**Figure 28.** Snow accumulation test (arc model) [First try].

Therefore, we reviewed the above-mentioned oil flow visualization results again and decided to investigate the cause of the increase in the amount of snow accumulated by the PA drive in the case of arc-shaped electrodes. The oil flow visualization results of the arc-shaped model are shown again in Figure 29. Focusing on the region where the arc-shaped electrode is parallel to the flow, the width of the region where the oil flow is deposited, which can be inferred to be the region where a streamwise vortex is formed along the electrode, is narrower. In the case of PA_ON, it was judged that the streamwise vortex was strengthened. This is supported by the fact that the red circle's triangular pattern of the oil flow becomes clearer with PA_ON. Therefore, it is presumed that the strengthening of this streamwise vortex increased the entrainment of the amount of snowfall, and in the case of the arc-shaped electrode, the amount of snowfall increased.

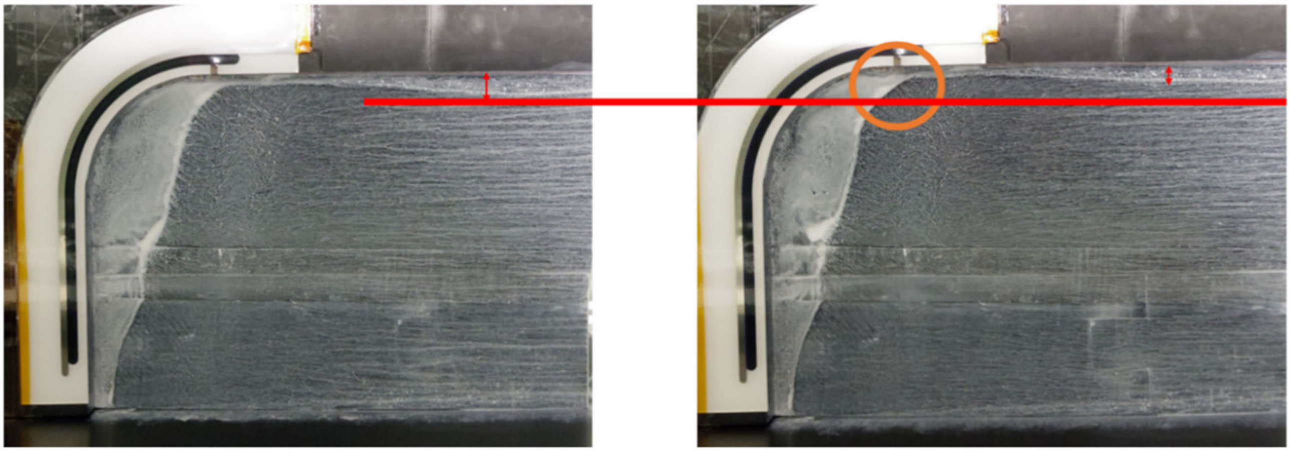

(**a**) PA_OFF (**b**) PA_ON

**Figure 29.** Oil flow visualization (Vertical Vortex).

To reduce the streamwise vortex effect on the arc-shaped separation region, we masked up to 45 degrees of the arc-shaped bend in the part parallel to the mainstream electrode. Figure 30 shows the masking processing status of the arc-shaped electrode.

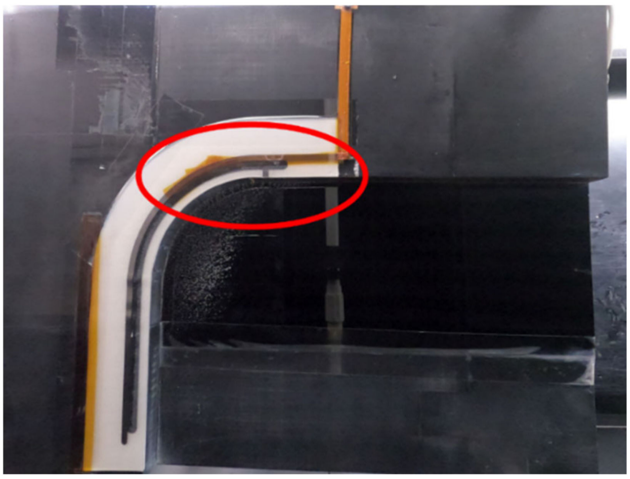

**Figure 30.** Masking process overview.

After the masking treatment, the snow accumulation test was performed again. Figures 31 and 32 show the masked PA_OFF and PA_ON snow accumulation tests, respectively. Tables 3 and 4 show the percentage decrease in each snow accumulation test. The threshold was set at 100. During the tests shown in Figures 31 and 32, the collection time was different, and the snow properties (density and humidity) were different, so the snow accumulation behavior changed. However, it was confirmed that the effect of suppressing snow accumulation could be obtained.

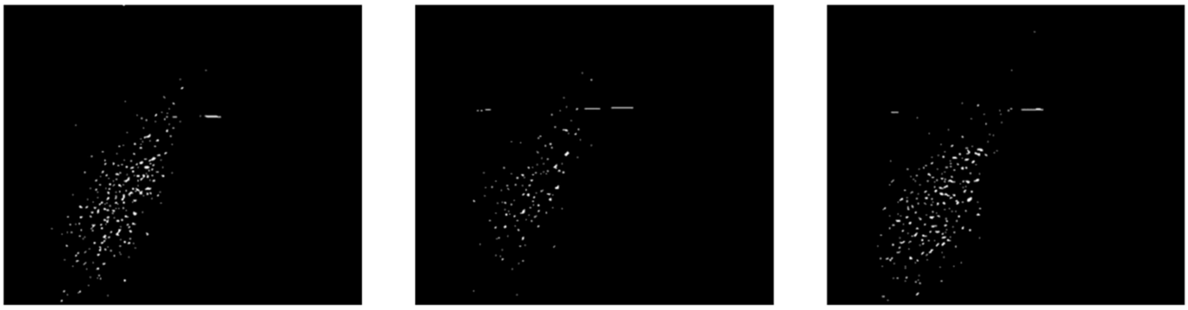

(**a**) PA_OFF (**b**) $D$ = 1.0% (**c**) $D$ = 15.0%

**Figure 31.** Snow accumulation test (arc model) [Result_1].

(**a**) PA_OFF (**b**) $D$ = 1.0% (**c**) $D$ = 15.0%

**Figure 32.** Snow accumulation test (arc model) [Result_2].

**Table 3.** Snow accumulation test (arc model) [Result_1].

| Duty | Off | 1.0% | 15.0% |
|---|---|---|---|
| White ratio [%] | 0.89 | 0.44 | 0.86 |
| Rate of decrease [%] | - | −50.56 | −3.37 |

**Table 4.** Snow accumulation test (arc model) [Result_2].

| Duty | Off | 1.0% | 15.0% |
|---|---|---|---|
| White ratio [%] | 3.22 | 2.59 | 2.59 |
| Rate of decrease [%] | - | −19.57 | −19.57 |

Furthermore, it was found that the effect of suppressing snow accumulation could be obtained at both $D$ = 1.0% and $D$ = 15.0%, even when the snow quality was different. In the oil flow visualization result of the standard model, the reattachment distance of $D$ = 1.0% is almost the same as in PA_OFF. Judging from these experimental facts, it can be inferred that the snow deposition suppression effect is caused by the formation of the acceleration region in the separated shear layer at the time of PA_ON.

## 4. Conclusions

Using a high-durability designed plasma electrode, the plasma actuation effect on a two-dimensional backward-facing step flow (standard model) and an arc-shaped three-dimensional backward-facing step flow (arc model) was investigated experimentally. The test using the standard model confirmed that the reattachment length decreased, and the separated shear layer accelerated when the PA was driven. At $Re = 4.1 \times 10^4$, based on the mainstream velocity and step height, it was confirmed that the reattachment length was most suppressed when the dimensionless frequency $fH/U$ = 0.32 and the duty ratio $D$ = 10 to 20%. Moreover, from the results of the snow accumulation test ($Re = 1.4 \times 10^4$), it became clear for the first time that the amount of snow accumulated in the two-dimensional backward-facing step flow could be reduced when the PA was driven. This is presumed to be due to the acceleration of the shear layer by the PA drive, which pushes off the snowfall flow. The test confirmed that accumulated snow could be reduced by more than 20%, even with the PA drive at $D$ = 1.0%. On the other hand, a comparison of the snow accumulated at the door corner of a railcar and the oil flow visualization results for the arc-shaped model shows that the snow accretion phenomenon on the railcar door is closely related to the separation phenomenon of the flow at the railcar door corner. It was confirmed that driving the entire arc-shaped PA electrode strengthened the longitudinal vortex in the part parallel to the mainstream due to plasma actuation, and as a result, the snow entrainment was strengthened, and the amount of snow accumulated increased. It was also confirmed that by masking the arc-shaped electrode parallel to the mainstream and using only the part perpendicular to the mainstream of the PA electrode, the amount of accumulated snow could be reduced by up to 20%. It has become clear that high-durability designed plasma electrodes can control the snowfall flow and reduce the amount of accumulated snow.

**Author Contributions:** Conceptualization, H.M.; methodology, H.M. and T.T. (Tasuku Tanaka); software, T.T. (Tasuku Tanaka), T.T. (Toshiki Takahashi) and H.M.; validation, T.T. (Tasuku Tanaka), T.T. (Toshiki Takahashi) and H.M.; formal analysis, T.T. (Tasuku Tanaka) and H.M.; investigation, T.T. (Tasuku Tanaka), T.T. (Toshiki Takahashi) and H.M.; resources, N.W., H.S., M.T. and T.C.; data curation, T.T.(Tasuku Tanaka), T.T. (Toshiki Takahashi), T.C. and H.M.; writing—original draft preparation, T.T. (Tasuku Tanaka); writing—review and editing, H.M.; visualization, T.T. (Tasuku Tanaka) and T.T. (Toshiki Takahashi); supervision, H.M.; project administration, H.M. and N.W.; funding acquisition, N.W., H.S. and H.M. All authors have read and agreed to the published version of the manuscript.

**Funding:** A part of the present research was supported by the Fukushima Prefecture renewable energy-related technology demonstration research support project.

**Data Availability Statement:** The data presented in this study are available on request from the corresponding author upon reasonable request.

**Acknowledgments:** The English translation of the text was supported by the devoted cooperation of Nakamura, K., who is a professor at the Hokkaido University of Science. Tajima, Y., provided guidance on the use of the power supply and production. The wind tunnel test was supported by the devoted coop-eration of Shibata, S., Yamazaki, T., Kobayashi, K., Iyobe, K., Sugawara, T., Muranaka, S., Uchida, S., Usutani, R., Naganuma, R., Uchino, N., and Matsunaga, J., who are students of the Department of Mechanical Engineering of the Hokkaido University of Science. We would like to express our gratitude.

**Conflicts of Interest:** The authors declare no conflict of interest.

## References

1. Corke, T.C.; Post, M.L.; Orlov, D.M. SDBD plasma enhanced aerodynamics: Concepts, optimization and applications. *Prog. Aerosp. Sci.* **2007**, *43*, 193–217. [CrossRef]
2. Touchard, G. Plasma actuators for aeronautics applications: State of art review. *Int. J. Plasma Environ. Sci. Technol.* **2008**, *2*, 1–25.
3. Moreau, E.; Debien, N.; Bénard, T.; Jukes, T.; Whalley, R.; Choi, K.-S.; Berendt, A.; Podlinski, J.; Mizeraczyk, J. Surface Dielectric Barrier Discharge Plasma Actuators. *ERCOFTAC Bull.* **2013**, *94*, 5–10.
4. Akbıyık, H.; Yavuz, H.; Akansu, Y.E. A Study on the Plasma Actuator Electrode Geometry Configurations for Improvement of the Aerodynamic Performance of an Airfoil. Strojniški vestnik. *J. Mech. Eng.* **2018**, *64*, 719–725.
5. Asaumi, N.; Matsuno, S.; Matsuno, T.; Sugahara, M.; Kawazoe, H. Multi-Electrode Plasma Actuator to Improve Performance of Flow Separation Control. *Int. J. Gas Turbine Propuls. Power Syst.* **2017**, *9*, 1–8. [CrossRef]
6. Wang, L.; Wong, C.W.; Alam, M.; Zhou, Y. Post-stall flow control using a sawtooth plasma actuator in burst mode. *Aerosp. Sci. Technol.* **2020**, *107*, 106251. [CrossRef]
7. Berendt, A.; Podliński, J.; Mizeraczyk, J. Multi-DBD plasma actuator for flow separation control around NACA 0012 and NACA 0015 airfoil models. *Prz. Elektrotech.* **2012**, *88*, 18–21.
8. Segawa, T.; Suzuki, D.; Fujino, T.; Jukes, T.; Matsunuma, T. Feedback Control of Flow Separation Using Plasma Actuator and FBG Sensor. *Int. J. Aerosp. Eng.* **2016**, *2016*, 8648919. [CrossRef]

9. Sato, S.; Enokido, T.; Ashikawa, K.; Matsubara, M.; Kanie, K.; Ohnishi, N. Development of a flexible dielectric-barrier-discharge plasma actuator fabricated by inkjet printing using silver nanoparticles-based ink. *Sens. Actuators A Phys.* **2021**, *330*, 112823. [CrossRef]
10. Ashpis, D.E.; Laun, M.C.; Griebeler, E.L. Progress Toward Accurate Measurement of Dielectric Barrier Discharge Plasma Actuator Power. *AIAA J.* **2017**, *55*, 2254–2268. [CrossRef] [PubMed]
11. Ashpis, D.E.; Laun, M.C. Dielectric Barrier Discharge Plasma Actuator Thrust Measurement Methodology Incorporating Antithrust Hypothesis. *AIAA J.* **2017**, *55*, 4181–4192. [CrossRef] [PubMed]
12. Matsunuma, T. Effects of Burst Ratio and Frequency on the Passage Vortex Reduction of a Linear Turbine Cascade Using a Dielectric Barrier Discharge Plasma Actuator. *Actuators* **2022**, *11*, 210. [CrossRef]
13. Zhang, X.; Cui, Y.D.; Tay, C.M.J.; Khoo, B.C. Flow field generated by a dielectric barrier discharge plasma actuator in quiescent air at initiation stage. *Chin. J. Aeronaut.* **2021**, *34*, 13–24. [CrossRef]
14. Chedevergne, F.; Casalis, G.; Léon, O.; Forte, M.; Laurendeau, F.; Szulga, N.; Vermeersch, O.; Piot, E. Applications of Dielectric Barrier Discharges and Plasma Synthetic Jet Actuators at ONERA. *Aerosp. Lab* **2015**, *AL10-06*, 1–10.
15. Benard, N.; Balcon, N.; Moreau, E. Electric wind produced by a surface dielectric barrier discharge operating in air at different pressures: Aeronautical control insights. *J. Phys. D Appl. Phys.* **2008**, *41*, 042002. [CrossRef]
16. Anderson, R.; Roy, S. Preliminary Experiments of Barrier Discharge Plasma Actuators using Dry and Humid Air. In Proceedings of the 44th AIAA Aerospace Sciences Meeting and Exhibit, Reno, NV, USA, 9–12 January 2006; p. 369.
17. Benard, N.; Balcon, N.; Moreau, E. Electric Wind Produced by a Surface Dielectric Barrier Discharge Operating Over a Wide Range of Relative Humidity. In Proceedings of the 47th AIAA Aerospace Sciences Meeting Including the New Horizons Forum and Aerospace Exposition, Orlando, FL, USA, 5–8 January 2009; p. 488.
18. Wicks, M.; Thomas, F.O. Effect of Relative Humidity on Dielectric Barrier Discharge Plasma Actuator Body Force. *AIAA J.* **2015**, *53*, 2801–2805. [CrossRef]
19. Lilley, A.J.; Roy, S.; Michels, L.; Roy, S. Performance recovery of plasma actuators in wet conditions. *J. Phys. D Appl. Phys.* **2022**, *55*, 155201. [CrossRef]
20. Fujii, K.; Asada, K. Resistance Reduction by Automotive Rear Flow Control Using DBD Plasma Actuators—Based on high-resolution simulation using HPC. *SENAC* **2020**, *53*, 15–24. (In Japanese)
21. Lai, C.; Fu, H.; Hu, B.; Ling, Z.; Jiang, L. Aerodynamic Drag Reduction and Optimization of MIRA Model Based on Plasma Actuator. *Actuators* **2020**, *9*, 64. [CrossRef]
22. Zainuddin, F.A.; Daud, N.M. A Review on Dielectric Barrier Discharge (DBD) Plasma Actuator in Aeronautics Applications. *J. Adv. Res. Fluid Mech. Therm. Sci.* **2018**, *48*, 125–132.
23. Keisar, D.; Hasin, D.; Greenblatt, D. Plasma Actuator Application on a Full-Scale Aircraft Tail. *AIAA J.* **2019**, *57*, 616–627. [CrossRef]
24. Sekimoto, S.; Kato, H.; Fujii, K.; Yoneda, H. In-Flight Demonstration of Stall Improvement Using a Plasma Actuator for a Small Unmanned Aerial Vehicle. *Aerospace* **2022**, *9*, 144. [CrossRef]
25. Xie, L.; Liang, H.; Han, M.; Niu, Z.; Wei, B.; Su, Z.; Tang, B. Experimental Study on Plasma Flow Control of Symmetric Flying Wing Based on Two Kinds of Scaling Models. *Symmetry* **2019**, *11*, 1261. [CrossRef]
26. Matsuda, H.; Tanaka, M.; Osako, T.; Yamazaki, K.; Shimura, N.; Asayama, M.; Oryu, Y. Plasma actuation effect on a MW class wind turbine. *Int. J. Gas Turbine Propuls. Power Syst.* **2017**, *9*, 47–52. [CrossRef]
27. Tanaka, M.; Kubo, N.; Kawabata, H. Plasma actuation for leading edge separation control on 300 kW rotor blades with chord length around 1 m at a Reynolds number around $1.6 \times 10^6$. *J. Phys. Conf. Ser.* **2020**, *1618*, 052013. [CrossRef]
28. Aono, H.; Fukumoto, H.; Abe, Y.; Sato, M.; Nonomura, T.; Fujii, K. Separated Flow Control of Small Horizontal-Axis Wind Turbine Blades Using Dielectric Barrier Discharge Plasma Actuators. *Energies* **2020**, *13*, 1218. [CrossRef]
29. Ogawa, T.; Asada, K.; Sekimoto, S.; Tatsukawa, T.; Fujii, K. Dynamic Burst Actuation to Enhance the Flow Control Authority of Plasma Actuators. *Aerospace* **2021**, *8*, 396. [CrossRef]
30. Van den Broecke, J. De-Icing Using Ns-DBD Plasma Actuators. Master's Thesis, Faculty of Aerospace Engineering, Delft University of Technology, Delft, The Netherlands, 2016.
31. Kolbakir, C.; Liu, Y.; Hu, H.; Starikovskiy, A.Y.; Miles, R. An Experimental Investigation on the Thermal Effects of NS-DBD and AC-DBD Plasma Actuators for Aircraft Icing Mitigation. In Proceedings of the AIAA SciTech Forum, AIAA Aerospace Sciences Meeting, Kissimmee, FL, USA, 8–12 January 2018.
32. Tian, Y.; Zhang, Z.; Cai, J.; Yang, L.; Kang, L. Experimental study of an anti-icing method over an air foil based on pulsed dielectric barrier discharge plasma. *Chin. J. Aeronaut.* **2018**, *31*, 1449–1460. [CrossRef]
33. Matsuda, H.; Chiba, T.; Yagami, M.; Tajima, Y.; Watanabe, N.; Sato, H.; Takeyama, M. Control of Snow Falling Flow around NACA0015 Blade using a Plasma Electrode with Weather Resistant Design. *J. Therm. Sci.* **2022**, *31*, 72–81. [CrossRef]
34. Matsuda, H.; Tanaka, M.; Goshima, S.; Okubo, T.; Atobe, T.; Kobayashi, H. Experimental Study on Flow Control of Separated Flows behind a Backward-Facing Step using Dielectric-Barrier-Discharge Plasma Actuator. *NAGARE* **2010**, *29*, 411–416. (In Japanese)
35. Urita, A.; Tanaka, S. Active Control of Separated Flows behind a Backward-Facing Step with Synthetic Jet (2nd Report, Study on Details of the Flow Structures and Consideration of Mechanism of Flow Modification from a Viewpoint of Coherent Structure). *Trans. JSME Part B* **2011**, *77*, 2422–2430. (In Japanese) [CrossRef]

36. Shibata, S.; Yamazaki, T.; Matsuda, H. Development of micro soap bubble generator for PIV tracer using home stereolithography 3D printer. In Proceedings of the 14th International Symposium on Particle Image Velocimetry, Chicago, IL, USA, 1–4 August 2021; p. 1.
37. Matsuda, H.; Uchida, T.; Tanaka, M.; Otomo, F.; Shimura, N.; Osako, T. Phase-locked PIV Measurements on Flow around Plasma Actuated 2D Wind Turbine Blade. *J. Gas Turbine Soc. Jpn.* **2014**, *42*, 535–540. (In Japanese)